High-frequency time-series autonomous observations of sea surface pCO_2 and pH

Yingxu Wu [1,2] Minhan Dai [1,3] Xianghui Guo [1,3]* Jinshun Chen,[1] Yi Xu,[1] Xu Dong,[4] Junwei Dai,[1]
Zhirong Zhang[1,3]

[1]State Key Laboratory of Marine Environmental Science, Xiamen University, Xiamen, China
[2]Key Laboratory of Global Change and Marine-Atmospheric Chemistry of Ministry of Natural Resources (MNR), Third Institute of Oceanography, MNR, Xiamen, China
[3]College of Ocean and Earth Sciences, Xiamen University, Xiamen, China
[4]Third Institute of Oceanography, Ministry of Natural Resources, Xiamen, China

Abstract

Carbon dioxide partial pressure (pCO_2) in surface water was continuously measured every 3 h from July 2012 to June 2013 using an autonomous pCO_2 system (MAPCO2) deployed on a moored buoy on the East China Sea shelf (31°N, 124.5°E). Sea surface pCO_2 and pH had the largest variations in summer, ranging from 215 to 470 μatm, and 7.941 to 8.263 (averagely 8.084 ± 0.080), respectively. They varied little in winter, ranging from 328 to 395 μatm, and 8.003 to 8.074 (averagely 8.052 ± 0.010), respectively. The seasonal average sea surface pCO_2 was respectively 335 ± 70 μatm, 422 ± 43 μatm, 362 ± 11 μatm, and 311 ± 59 μatm in summer, autumn, winter, and spring, and was overall undersaturated with respect to atmosphere on a yearly basis. Although the average sea surface pCO_2 in summer was below the atmospheric level, the net CO_2 flux has suggested a CO_2 source status due to the influence of typhoon. Our observation thus demonstrated the significant, even dominant impact of episodic typhoon events on surface ocean CO_2 chemistry and air–sea CO_2 gas exchange, which would be impossible to capture by shipboard observation. The high wind stress and curl associated with the northward movement of typhoon induced complex sea surface water movement, vertical mixing, and subsequent biological drawdown, which differed in pre-, onset, and post-typhoon stages. Based on our estimates, the degassing fluxes during typhoon reached as high as 82 mmol m^{-2} CO_2 and 242 mmol m^{-2} CO_2 in summer and autumn, respectively, accounting for twice as large as the summer CO_2 sink during non-typhoon period, and 28% of the total CO_2 source in autumn.

Despite having a relatively modest surface area, the coastal ocean plays a considerable role in the uptake of atmospheric CO_2 (0.2–0.5 Pg C yr^{-1}, 1 Pg = 10^{15} g) (Bauer et al. 2013; Dai et al. 2013; Laruelle et al. 2014). The large uncertainties associated with estimations of coastal air–sea CO_2 fluxes, which often possess highly dynamic ranges, are largely due to the poor spatial, and especially the temporal, coverage of field observations and measurements (Gruber 2015). As a consequence, the current accuracy of coastal ocean carbon budgets remains insufficient to be included in the earth system model for reliably predicting future climate changes (Cai 2011; Gruber 2015).

Long-term time-series observations (e.g., Bates et al. 2014; Sutton et al. 2014a,b) are critically needed to decipher the dynamics of the oceanic environment, and to detect changes in the global ocean carbon cycle, due to both natural processes and anthropogenic perturbations, in the broad context of global warming and ocean acidification. Given the highly temporal and spatial heterogeneity of coastal oceans (Chen and Borges 2009; Dai et al. 2013; Gruber 2015), as a consequence of large, variable riverine inputs of carbon and nutrients, and dynamic exchange with the open ocean, it is also of critical importance to carry out long-term high-frequency observations to better understand the coastal ocean CO_2 system (Bates et al. 2014; Xue et al. 2016; Li et al. 2018).

Both physical and biological processes are known to affect CO_2 dynamics, including the partial pressure of CO_2 (pCO_2) in coastal waters over various time scales spanning from diurnal to seasonal changes. These processes can be further divided into those which lower sea surface pCO_2, such as the biological removal of carbon fueled by riverine or subsurface

*Correspondence: xhguo@xmu.edu.cn

inputs of nutrients (Chen et al. 2012; Wang et al. 2017*a,b*; Li et al. 2018), and those which increase pCO$_2$, such as vertical mixing driven by episodic strong winds (Bates et al. 1998; Nemoto et al. 2009) or the seasonal collapse of surface stratification (Zhai and Dai 2009) resulting in the supply of subsurface high-CO$_2$ waters into the surface mixed layer. In addition, temperature also exerts a dominant control on sea surface pCO$_2$ variability by affecting CO$_2$ solubility (Weiss 1974).

The East China Sea is characterized by significant terrestrial inputs from one of the world's largest rivers, the Changjiang, and dynamic exchanges with complex water masses (Chen 2009), for example, from the Yellow Sea and the Kuroshio Current (Chen and Wang 1999). Located in the temperate zone of the western Pacific Ocean, the East China Sea is regularly impacted by western Pacific tropical cyclones during warm seasons (D'Asaro et al. 2011). The East China Sea and its estuarine and nearshore regions have been a focus of coastal air–sea CO$_2$ exchange studies in the past decades (e.g., Zhai and Dai 2009; Guo et al. 2015; Chou et al. 2017). Subject to large spatial and temporal variabilities, this coastal region has distinct seasonal patterns, with a warm and productive summer and a cold and less productive winter. In the East China Sea, areas located between 28.5–33.0°N and 122.0–126.0°E exhibit the largest seasonal variations in sea surface temperature, salinity, and pCO$_2$, as a consequence of biological CO$_2$ uptake during warm seasons, ventilation in autumn, and cooling in winter (Guo et al. 2015).

Most of the previous studies in the East China Sea are based on shipboard observations (e.g., underway or discrete measurements), with a focus on mapping the spatial dynamics of pCO$_2$ (Zhai and Dai 2009; Tseng et al. 2011; Guo et al. 2015). However, these studies are limited in terms of temporal resolution, leading to large uncertainties in estimations of air–sea CO$_2$ fluxes and an incomplete understanding of their underlying processes (Chou et al. 2009*b*; Nemoto et al. 2009). For instance, Li et al. (2018) investigated the dependence of air–sea CO$_2$ fluxes on sampling frequency (e.g., every 3 d, weekly, and monthly) on the inner shelf of the East China Sea, showing that the potential error in estimated fluxes increases sharply with decreasing sampling frequency. Even weekly sampling is capable of introducing flux biases of up to ± 63% (Li et al. 2018). Time-series studies in other coastal waters around the world have also demonstrated the importance of high-frequency observations to accurately estimate air–sea CO$_2$ fluxes (Dai et al. 2009). High-frequency pCO$_2$ values recorded in the Bay of Brest (Bozec et al. 2011) suggested that sampling only during the day or night could introduce an 8–36% bias on air–sea CO$_2$ monthly estimates. Adding in additional complexity, episodic events such as typhoons can promote vertical mixing (e.g., Price 1981; Nemoto et al. 2009), thereby introducing CO$_2$-rich subsurface water into the surface layer. Continuous observations by Nemoto et al. (2009) have successfully captured the dynamics of sea surface pCO$_2$ during the passage of three typhoons across the East China Sea. The efflux of CO$_2$ induced by the severe weather increased by 150% over normal

warm season conditions (Nemoto et al. 2009). Similar to Nemoto et al. (2009), most of the previous continuous observations (e.g., Bond et al. 2011; Wada et al. 2011; Sun et al. 2014) only focused on the uplifting process during typhoon, without paying enough attention to the typhoon-induced phytoplankton blooms (Hung and Gong 2011; Lin 2012; Ye et al. 2013). Moreover, although efforts have been put into understanding the biogeochemical responses of phytoplankton flourish after the passage of typhoon, few of them have concentrated on the interaction between wind, sea surface pCO$_2$, air–sea CO$_2$ flux, and chlorophyll *a* (Chl *a*), not to mention the evolution of upper ocean response throughout the typhoon period (i.e., pre-typhoon, during typhoon, and post-typhoon). As a consequence, for regions vulnerable to typhoons such as the East China Sea, the demand for buoy-based time-series observations has increased.

In this study, we report here the first year-round high-frequency (3-h intervals) data set with a combination of physical, biological, and chemical parameters (such as sea surface temperature, sea surface salinity, surface wind velocity, Chl *a*, pCO$_2$, and pH), from 28 July 2012 to 01 June 2013 based on a buoy system deployed on the East China Sea shelf. We aim to investigate the seasonal evolution of sea surface pCO$_2$ and pH along with other associated parameters. In particular, we focused on the temporal variability of sea surface pCO$_2$ and air–sea CO$_2$ gas exchange during episodic events (e.g., typhoon, bloom), in order to fill the knowledge gaps from traditional ship-based surveys. A novel conclusion of this study is that three stages of typhoon are identified, during which the surface wind field interacts with the observing system, resulting in different responses of surface CO$_2$ chemistry.

Materials and methods

Study area

The East China Sea is one of the major marginal seas of the Pacific Ocean, and one of the most productive shelf regions in the world (Gong et al. 2003; Hung et al. 2003). It is characterized by significant riverine inputs from the Changjiang River, which ranks 4th globally in terms of freshwater discharge (Dai and Trenberth 2002), as well as exchange with the Kuroshio along the eastern boundary of the outer shelf (Chen and Wang 1999). The major surface water masses in the East China Sea (Chen 2009) include (1) the Changjiang River plume, also known as Changjiang Diluted Water, which flows northeastward in summer and southwestward in winter (Lee and Chao 2003; Bai et al. 2014), (2) East China Sea Coastal Water, which flows southward during winter monsoons and northward during summer monsoons, (3) the Taiwan Warm Current, which flows northward all year round, (4) Yellow Sea Coastal Water, which flows generally southeastward; and (5) the Kuroshio Current, which generally flows along the 100–200 m isobaths in the East China Sea and leaves the continental slope at 30°N and 128–129°E (Fig. 1).

Previous studies on the East China Sea carbon cycle have suggested that the East China Sea acts as an annual net CO_2 sink, yet with remarkable seasonal and spatial variability (Guo et al. 2015, and references therein). Across the entire East China Sea shelf, the core area of the plume-influenced region in the outer Changjiang estuary (28.5–33.0°N, 122.0–126.0°E) in summer has the lowest sea surface pCO_2 and the largest variability in air–sea CO_2 fluxes (ranging from 1.6 to 10.2 mmol m^{-2} d^{-1}; Guo et al. 2015). The highly productive Changjiang River plume, especially in summer, can promote photosynthesis in the outer estuary (Gong et al. 2003; Tseng et al. 2011; Chen et al. 2012) where our buoy is located (31°N, 124.5°E, $\sim$ 300 km east of Shanghai, with a water depth of $\sim$ 60 m; Fig. 1). The CO_2 fluxes over the rest of the East China Sea shelf are less variable (Guo et al. 2015).

Measurements and equipment

Time-series data were collected from 28 July 2012 to 01 June 2013 by sensors (monitoring systems) deployed on a buoy constructed by Xiamen University. Sensors were mounted at depth of 0.5 m, including a Battelle pCO_2 monitoring system with 3-h sampling intervals, a SeaFET Ocean pH sensor with 1-h sampling intervals, a SBE 37-SI conductivity and temperature sensor with 10-min sampling intervals, and a WET Labs fluorescence sensor to measure turbidity (nephelometric turbidity units [NTU]) and Chl a at 1-h intervals. Wind velocity and barometric pressure were obtained by a weather station (Model 05106 and 61302V, Young Company, U.S.A.) equipped on the buoy at $\sim$ 10 m above the sea surface. Sensors were connected to the data acquisition system on the buoy, and data were sent to the land-based laboratory in real-time by satellite transmission.

The Battelle CO₂ system

A Battelle CO_2 monitoring system was deployed for measuring air and surface seawater pCO_2 values, which were determined by a Li-Cor 820 nondispersive infrared (NDIR) gas analyzer contained in the Electronics Assembly. The Battelle CO_2 system is the same one as the widely used Moored Autonomous pCO_2 (MAPCO2) system, as described in Sutton et al. (2014b). The pCO_2 monitor cycles a closed circuit of air through the surface seawater via an "h" shaped tube assembly to reach equilibrium of CO_2 with the air, then the equilibrated air is analyzed to determine the CO_2 mole fraction (xCO_2).
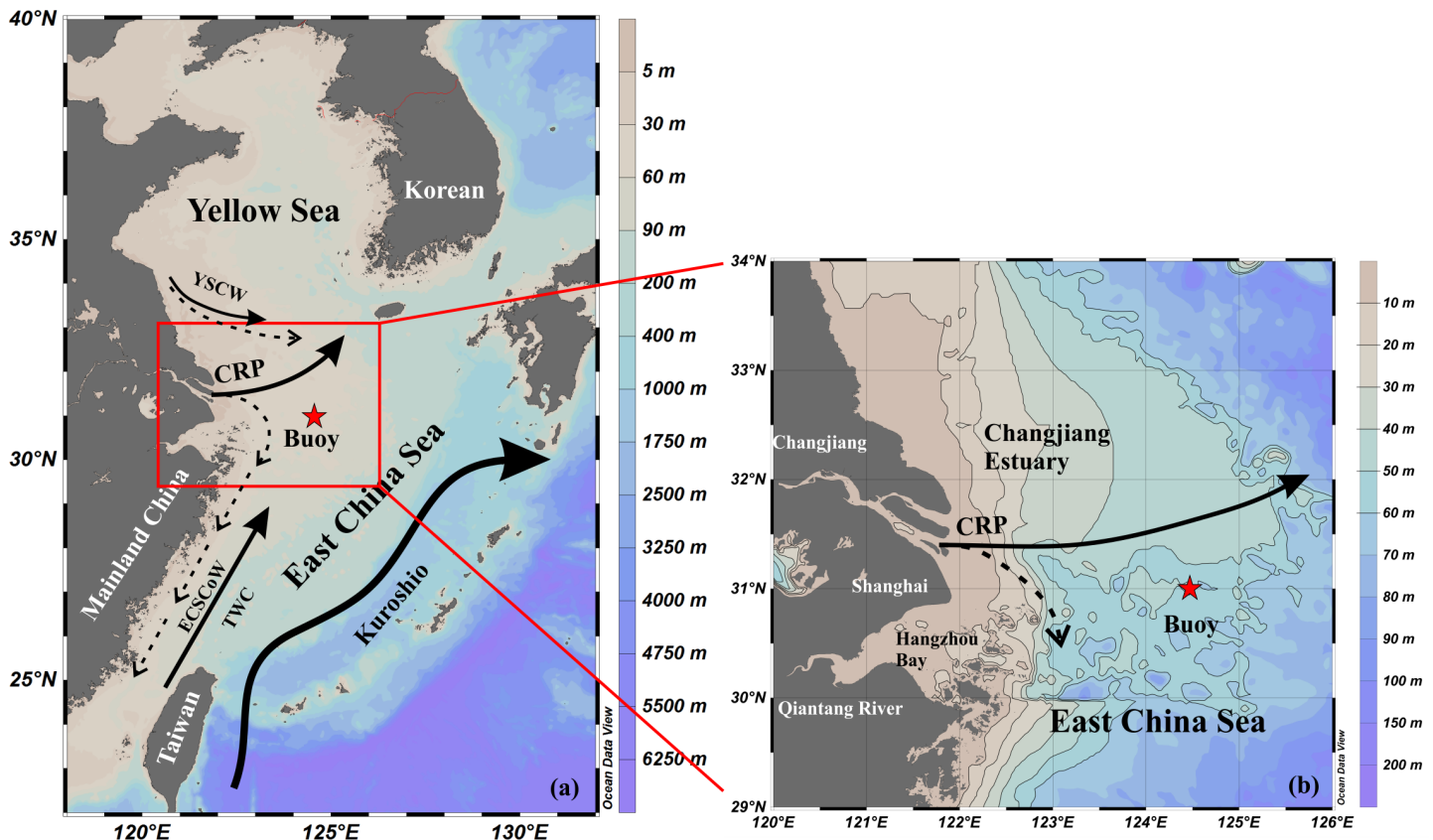

Fig. 1. Maps of the East China Sea. The red star shows the location of the buoy site at 31°N, 124.5°E. The main currents in the East China Sea in summer and winter are shown; the Kuroshio, Taiwan Warm Current (TWC), East China Sea Coastal Water (ECSCoW), Changjiang River plume (CRP), and Yellow Sea Coastal Water (YSCW). The solid arrows represent currents in summer, and the dashed arrows represent currents in winter, except for the Kuroshio and TWC which flow northward all year round. Note that the colormaps in (**a**) and (**b**) are in different scales.

After the seawater xCO$_2$ measurement, air xCO$_2$ is measured by directly drawing an air sample from above the sea surface (*see* Sutton et al. 2014*b* for more detail). Since the "h" shaped pipe is the only part that contacts seawater and is made of a copper nickel alloy, the CO$_2$ monitor has a good performance in resisting biological fouling. The CO$_2$ measurements are quality-controlled by a two-point auto-calibration prior to every sample using a zero reference (ambient air that has passed through a soda lime canister to remove all CO$_2$) and a span reference (stored dry air with a precisely known xCO$_2$). The CO$_2$ span reference we used in this study had a xCO$_2$ value of 458.81 μmol mol^{-1}, of World Meteorological Organization level. The uncertainty of the calculated pCO$_2$ (Eq. 1) by the MAPCO$_2$ system is reported to be < 2 μatm (Sutton et al. 2014*b*; with a precision of < 0.6 μmol mol^{-1} for the measured xCO$_2$ values).

Water pCO$_2$ was calculated from the xCO$_2$ value in dry air equilibrated with surface water and the barometric pressure (P) after correcting for the vapor pressure (P_{H2O}) of water at 100% relative humidity (Weiss and Price 1980):

$$p\text{CO}_2 = (P - P_{H2O}) \times x\text{CO}_2 \qquad (1)$$

pCO$_2$ in the air was calculated similarly based on measured xCO$_2$ values in the air and the barometric pressure, using a formula similar to Eq. 1.

The pH sensor

The SeaFET Ocean pH sensor is an autonomous data logger based on a Honeywell Durafet® pH sensor (Martz et al. 2010). The primary element of SeaFET is an ion-sensitive field effect transistor (ISFET), which produces robust, stable, and precise measurements. Martz et al. (2010) evaluated the performance of the ISFET sensor in a number of different situations (e.g., a temperature-controlled calibration vessel, the Monterey Bay Aquarium Research Institute [MBARI] test tank, shipboard underway mapping and a surface mooring): it showed a short-term precision of ± 0.0005 over periods of several hours and a stability of better than ± 0.005 over periods of weeks to months. A comparison of high-resolution time-series data of upper ocean pH using the SeaFET pH sensors was provided by Hofmann et al. (2011). The experiments were conducted across a variety of ecosystems ranging from polar to tropical, open-ocean to coastal, and kelp forest to coral reef. It was suggested that the pH uncertainty is higher at dynamic sites due to the intense gradients, where the observed sampling errors ranged from ± 0.0007 to ± 0.015. However, in many instances, the uncertainty was expected to be better than ± 0.01. In addition, biofouling was believed to compromise the data quality during deployments over 2 months in high-fouling environments, therefore, we protected the sensor with a perforated copper anti-fouling guard. pH values in this study are all on total scale at in situ temperature.

Data quality assessment by shipboard measurements

To assess the data quality of the MAPCO2 system, we compared buoy and shipboard measurements of sea surface pCO$_2$ and other parameters (Table 1) at the beginning and end of the observation, respectively. The shipboard measurements in July 2012 collected discrete samples for total alkalinity (TA), dissolved inorganic carbon (DIC), and Chl *a* (Table 1). TA and DIC samples were measured to calculate pCO$_2$ and pH using the Excel program "CO2SYS" (Pierrot et al. 2006). The dissociation constants for carbonic acid were taken from Mehrbach (1973) as refitted by Dickson and Millero (1987), the dissociation constant for sulfate was taken from Dickson (1990), the total boron-salinity relationship was from Lee et al. (2010), and pH values are given on the total hydrogen scale at in situ temperature. TA was measured using an automated Gran acidimetric titration using an Apollo Alkalinity Titrator (Model AS-ALK 1+), with a precision of $\pm 0.1\%$ (Cai et al. 2004). DIC was measured using an Apollo DIC Analyzer (Model AS-C3) with a precision of $\pm 0.1\%$ (Cai et al. 2004). Reference materials from Andrew G. Dickson's laboratory at Scripps Institution of Oceanography were used to calibrate the system to an accuracy of ± 2 μmol kg^{-1}.

The shipboard measurements in July 2013 were made using the underway pCO$_2$ system with a shower-head water–air equilibrator and a NDIR detector as described in detail in Zhai et al. (2005). The NDIR detect (Li-Cor 7000) were calibrated every 8 h using a wide range of CO$_2$ gas standards that covered the pCO$_2$ variability during the cruises. The overall uncertainty of the CO$_2$ measurements was $< 1\%$ as constrained by the standard gases. Sea surface temperature and salinity were determined by a Yellow Springs Instrument meter (YSI 6600), which was combined with the continuous pCO$_2$ system. Due to the severe weather conditions, the comparison was made at nearshore site outside Qushan Island (at 30.44°N, 122.28°E) when the buoy was dragged back, where relatively higher pCO$_2$ values (~ 800 μatm) were found (Table 1). Shipboard measurements of pCO$_2$ in July 2013 were performed over the same site (30.44°N, 122.28°E) at 0.5-h intervals.

The overall offset of the buoy measurements from the shipboard measurements was -0.013 ± 0.010 for pH, 0.045 ± 0.075 μg L^{-1} for Chl *a*, and $< 2\%$ for pCO$_2$ (Table 1). It is also noteworthy that the average offsets in pCO$_2$ in 2012 and 2013 were 2.1% and 1.6%, respectively, showing a good consistency with respect to time (i.e., no significant drift). This indicates a reasonably good accuracy of the buoy measurements. A good agreement of pCO$_2$ between the MAPCO2 system and shipboard measurements was also found by Liu et al. (2019) in the adjacent area to our study site.

Tropical depression data acquisition

The tropical depression (typhoon) data in this study corresponds to track data from Unisys Weather (http://weather.

Table 1. Comparison of surface seawater pCO_2, pH, and Chl *a* between buoy and shipboard measurements during the deployment (at the study site 31°N, 124.5°E in 2012) and the recovery of buoy (at 30.44°N, 122.28°E in 2013). Date format: year/month/day.

	Buoy observations					Shipboard observations						
Date and time	pCO_2 (µatm)	pH	Chl *a* (µg L⁻¹)	SST (°C)	SSS	pCO_2* (µatm)	pH*	Chl *a* (µg L⁻¹)	TA (µmol kg⁻¹)	DIC (µmol kg⁻¹)	SST‡ (°C)	SSS‡
2012/07/27 23:00	332	8.087	0.58	29.48	30.68	326	8.111	n.m.	2207.3	1868.5	29.48	30.68
2012/07/28 04:00	444†	8.142†	0.28	29.23	30.56	271	8.174	0.22	2203.7	1829.1	29.23	30.56
2012/07/28 05:00	283	8.144	0.62	29.16	30.58	288	8.150	n.m.	2185.4	1828.6	29.16	30.58
2012/07/28 06:00	277	8.150	0.33	29.03	30.61	283	8.158	0.31	2193.7	1831.7	29.03	30.61
2012/07/28 07:00	340	8.150	0.27	29.03	30.58	331	8.106	0.31	2197.4	1868.1	29.03	30.58
2013/07/29 18:30	798	n.m.	n.m.	27.47	28.85	804	n.m.	n.m.	n.m.	n.m.	27.01	29.07
2013/07/29 19:00	793	n.m.	n.m.	27.28	28.78	802	n.m.	n.m.	n.m.	n.m.	26.90	29.10
2013/07/29 19:30	795	n.m.	n.m.	27.24	28.77	803	n.m.	n.m.	n.m.	n.m.	26.96	29.05
2013/07/29 20:00	786	n.m.	n.m.	27.19	28.80	807	n.m.	n.m.	n.m.	n.m.	26.99	29.05
2013/07/29 20:30	790	n.m.	n.m.	27.15	28.81	811	n.m.	n.m.	n.m.	n.m.	26.93	29.06

n.m., not measured; SSS, sea surface salinity; SST, sea surface temperature.

*Data in year 2012 were computed with CO2SYS (Pierrot et al. 2006) based on TA and DIC measurements; data in 2013 were underway pCO_2 measurements. pCO_2 measurements in July 2013 were performed at the site (30.44°N, 122.28°E) at 0.5-h intervals.

†The large discrepancy was supposed to relate to the movement of the buoy while sampling.

‡Due to sampling restrictions, we used the buoy-measured SST and SSS to calculate the carbonate system parameters collected in 2012.

unisys.com/hurricane/) based on the U.S. Joint Typhoon Warning Center. The track data consist of the location, intensity, and status of the typhoon center at 6-h intervals.

Computational methods

In order to distinguish thermal and nonthermal effects on seawater pCO_2, we used the relationships predicted by Takahashi et al. (1993), assuming that the temperature dependence of pCO_2 for a parcel of seawater with a constant chemical composition be expressed as $\partial \ln pCO_2 / \partial T = 0.0423°C^{-1}$. To remove the temperature effect, the observed pCO_2 value was normalized to an average temperature ($NpCO_2$) as:

$$NpCO_2 = (pCO_2)_{obs} \times \exp[0.0423 \times (T_{ave} - T_{obs})], \tag{2}$$

where the subscripts "ave" and "obs" represent the average and observed values, respectively. T denotes temperature.

The net air–sea CO_2 flux is estimated using the air–sea pCO_2 difference and the gas transfer coefficient:

$$F_{CO2} = k \times \alpha \times (pCO_{2,sw} - pCO_{2,air}), \tag{3}$$

where k is the CO_2 gas transfer velocity, α is the solubility of CO_2 in seawater (Weiss 1974), and subscripts "sw" and "air" denote pCO_2 of seawater and atmosphere, respectively. A positive flux indicates a net CO_2 exchange from seawater to atmosphere, while a negative flux indicates a net CO_2 exchange from atmosphere to seawater. The gas transfer velocity was estimated using the wind velocity relationship from Sweeney et al. (2007), expressed as:

$$k = 0.27 \times (u_{10})^2 \times (Sc/660)^{-1/2} \tag{4}$$

where u_{10} is the wind velocity at 10 m above the sea surface; and the Schmidt number (Sc) is temperature-dependent for CO_2 in seawater, computed from in situ temperature (Wanninkhof 1992).

On the basis of Eq. 3, we adapted it to examine how the variations in different terms, that is, gas transfer coefficient, sea surface pCO_2, and atmospheric pCO_2, would affect the CO_2 flux estimation:

$$F_{CO2} = K \times (pCO_{2,sw} - pCO_{2,air}), \tag{5}$$

where K is the CO_2 gas transfer coefficient, $K = k \times \alpha$.

The differential of the CO_2 flux, with respect to time, can be written as:

$$\frac{\partial F}{\partial t} = \frac{\partial K}{\partial t} \times \Delta pCO_2 + \frac{\partial pCO_{2,sw}}{\partial t} \times K - \frac{\partial pCO_{2,air}}{\partial t} \times K, \tag{6}$$

where the first term on the right-hand side of Eq. 6 represents the variation in CO_2 fluxes attributed to changes in the gas transfer coefficient (wind velocity dominated), and the rest two terms represent CO_2 flux variations attributed to changes in $pCO_{2,sw}$ and $pCO_{2,air}$.

Results

Hydrological settings

The time-series observation (Fig. 2a,b) shows the strong seasonal variations in sea surface temperature and salinity (hereafter referred to simply as temperature and salinity) at the study site. Seasons are defined as each consisting of 3 months, for instance, summer from June to August. During the observation, temperature decreased from 28.4 ± 1.3°C in summer to 22.6 ± 2.1°C in autumn, to the lowest 13.0 ± 2.5°C in winter, and increased to 13.5 ± 3.5°C in spring. Salinity changes also indicated the seasonal pattern. The study site is located in a river-dominated system (Tseng et al. 2011), subjected to seasonally variable freshwater discharge from the Changjiang (Zhai et al. 2007), thus resulting in a large fluctuation in salinity in summer. The study area is also subjected to significant surface stratification in spring and summer and well-mixed condition in seasons after (Zhai and Dai 2009). The average summer salinity was 31.8 ± 1.4 and reached a low value of 28.5, comparable to the previous observation (salinity of around 32.3 in summer in Chou et al. 2009*a*) identifying the signal of Changjiang River plume. Salinity variations in autumn and spring (Fig. 2b) also implied the influence of freshwater runoff, with average values of 32.7 ± 0.6 and 32.3 ± 0.9, respectively. Salinity in winter was relatively constant and higher, and the winter average value (32.7 ± 0.3) ranked the highest among the seasons.

It is noteworthy that the observations in this study started in late July 2012 and ended in early June 2013, so data in June and July were missing during the "continuously" observed annual cycle. This may potentially influence the understanding of the seasonal cycle of the surface seawater pCO$_2$ and subsequent estimation of the annual air–sea CO$_2$ flux (more details in "Air–sea CO$_2$ fluxes" section).

Biogeochemical parameters

During the observation period, sea surface pCO$_2$ (pCO$_{2,sw}$) exhibited significantly large variations (Fig. 2c; Table 2). It showed an overall increasing trend to above the atmospheric level from summer to mid-autumn, despite being characterized by dramatic fluctuations, followed by a transitional period from CO$_2$ supersaturation to undersaturation in late autumn. Afterward, it stayed fairly constant until late winter. There was a sharp decrease in pCO$_{2,sw}$ in spring, where it reached the lowest value throughout the observation period. The highest pCO$_{2,sw}$ value of 513 μatm was observed in late October 2012, while its lowest value of 167 μatm was observed in late April 2013.

In contrast to sea surface pCO$_2$, atmospheric pCO$_2$ (pCO$_{2,air}$) had its maxima in winter and minima in summer (Fig. 2c), behaving much more stable than pCO$_{2,sw}$, with an annual average value of 380 μatm.

pH closely mirrored pCO$_{2,sw}$ (Fig. 2d), with the lowest values of 7.976 ± 0.026 observed in October and the highest values of 8.070 ± 0.043 in April (Table 2). Turbidity (Fig. 2f) had several peaks during summer and autumn coinciding with the peaks in wind velocity (Fig. 2e): however, the timing the Chl *a* peaks (Fig. 2f) did not correspond exactly to those in turbidity or wind velocity, often having a lag of a few days.

Dynamics of sea surface pCO$_2$ and pH over different timescales

On the seasonal timescale, the average pCO$_{2,sw}$ in summer was 335 ± 70 μatm, relatively lower than the average atmospheric pCO$_2$ (pCO$_{2,air}$) value of 369 ± 4 μatm, with considerably large variations. In autumn, the study site became a CO$_2$ source. pCO$_{2,sw}$ exceeded the atmospheric level, and reached its maximum at 422 ± 43 μatm. In winter, pCO$_{2,sw}$ decreased sharply to 362 ± 11 μatm, and the study site turned into a CO$_2$ sink. In spring, due to the sudden drop in values starting in May, pCO$_{2,sw}$ was reduced to 311 ± 59 μatm, the lowest seasonal average value. In contrast to pCO$_{2,sw}$, pH exhibited an opposite seasonal trend: it was highest in spring (pH = 8.097 ± 0.076), followed by summer (pH = 8.084 ± 0.080) and then winter (pH = 8.052 ± 0.010), and reached its minimum in autumn (pH = 7.998 ± 0.039). Surface water pH showed the largest seasonal fluctuations in spring and summer, and remained fairly constant in autumn and winter.

In addition to the large seasonal variability, pCO$_{2,sw}$ and pH were also highly variable at the intraseasonal timescale, especially during warm seasons (Table 2). Both pCO$_{2,sw}$ and pH had the largest diurnal variations in August and September of 2012 and May of 2013, when the seasonal fluctuations of these parameters were also the largest.

Dynamics of sea surface pCO$_2$ and associated parameters during typhoon

During the observation, a total of five typhoons (*Damrey*, *Haikui*, *Bolaven*, *Tembin*, *Sanba*) passed by the buoy site in summer and autumn 2012 with a distance as close as 50 km (i.e., *Tembin*, *see* Fig. 3). All typhoons, except *Haikui* which was 350 km far away from the buoy (Fig. 3), exerted great impacts on the study site as seen from sea level pressure (hereafter referred to simply as pressure unless otherwise specified, measured by weather station at the buoy), wind velocity and turbidity (Figs. 4–6). *Damrey* was formed on 28 July, and traveled across the study site from its east on 02 August. *Tembin* and *Bolaven* were formed on 19 August and 20 August, respectively. However, *Bolaven* arrived at the buoy location approximately 2 d earlier than *Tembin*, and had a larger wind radius. *Bolaven* passed 110 km northeast of the buoy site at a translation speed (describing how fast a typhoon was moving) of 8.3 m s^{-1}, and *Tembin* passed 50 km east of the buoy site with a translation speed of 11.7 m s^{-1}. *Sanba* formed on 10 September, and passed by the buoy on 17 September from its southeast with a translation speed of 9.0 m s^{-1}. The sensors on the buoy kept working (Figs. 4–6) without significant
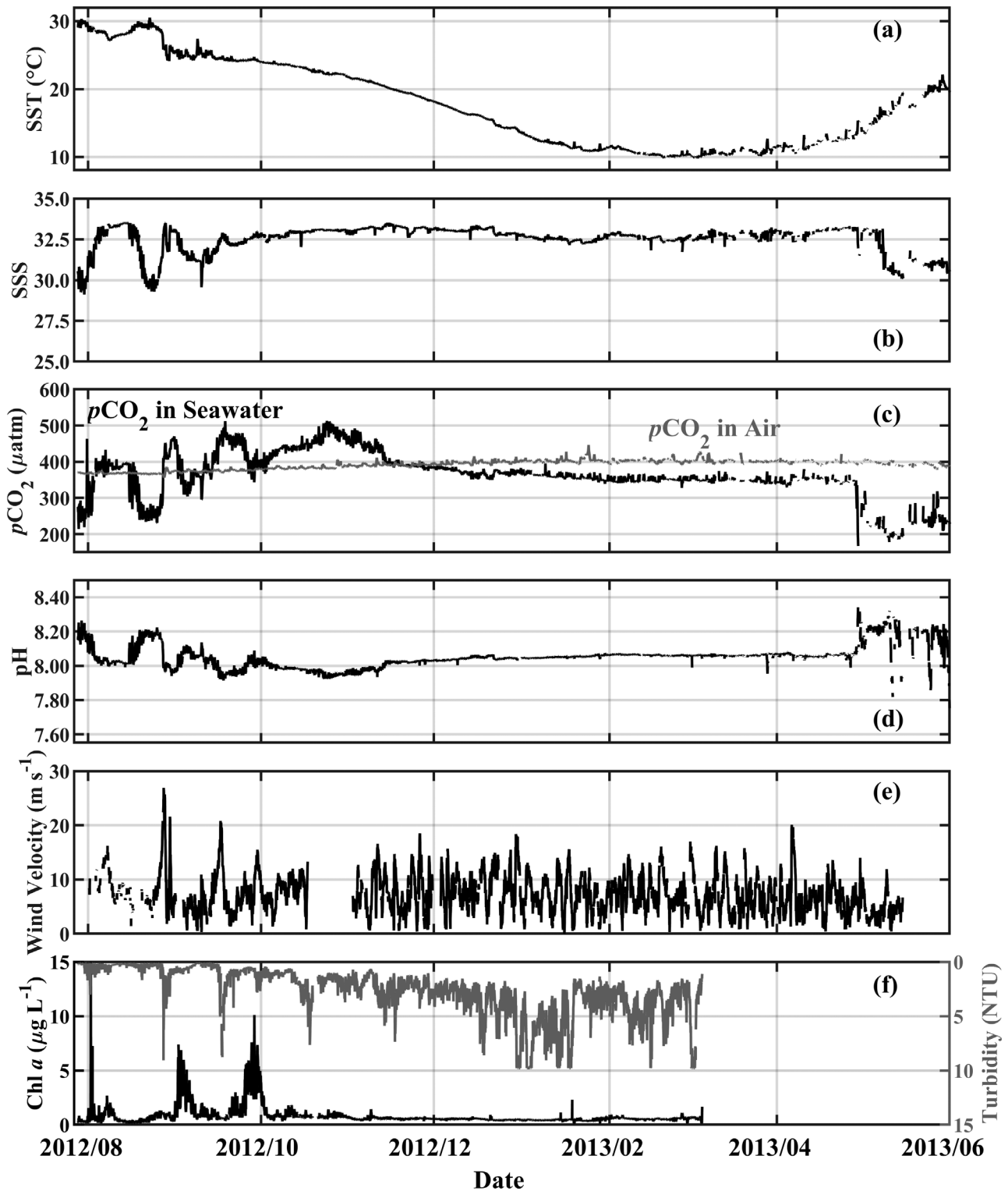
Fig. 2. Time-series of surface properties (**a:** SST, **b:** SSS, **c:** pCO_2, **d:** pH, **e:** wind velocity, and **f:** Chl *a*) observed at the buoy site from July 2012 to June 2013. SSS, sea surface salinity; SST, sea surface temperature.

interruptions during the typhoon's passages, which further demonstrated the high performance of the buoy system under severe weather conditions.

The occurrence of *Damrey* has caused a drop in pressure by around 1 kPa and an increase in turbidity by 2.5 NTU (Fig. 4a,d), whereas the pressure drop during *Haikui* was

Table 2. Summary of the monthly average value and averaged monthly diurnal range of surface $pCO_{2,sw}$, $pCO_{2,air}$, sea surface temperature (SST), salinity (SSS), pH, and Chl *a* at the study site.

| | Monthly average value (average ± standard deviation) | | | | | | Average monthly diurnal range | | | | | |
Month	$pCO_{2,sw}$ (μatm)	$pCO_{2,air}$ (μatm)	SST (°C)	SSS	pH	Chl *a* (μg L^{-1})	$pCO_{2,sw}$ (μatm)	$pCO_{2,air}$ (μatm)	SST (°C)	SSS	pH	Chl *a* (μg L^{-1})
2012/08	348±67	369±4	28.1±1.3	32.1±1.3	8.073±0.076	0.71±0.80	55	5.3	0.78	1.02	0.06	1.4
2012/09	404±50	375±3	24.7±0.6	32.0±0.6	8.016±0.049	2.11±1.74	51	4.8	0.68	0.54	0.07	2.4
2012/10	448±30	382±4	23.0±0.7	32.9±0.2	7.976±0.026	0.90±0.37	29	8.0	0.24	0.23	0.03	0.6
2012/11	415±32	391±4	20.1±1.1	33.2±0.2	8.003±0.028	0.58±0.10	20	7.2	0.18	0.28	0.02	0.3
2012/12	371±9	398±5	15.9±1.3	33.0±0.2	8.043±0.010	0.51±0.07	12	7.7	0.21	0.28	0.01	0.2
2013/01	360±8	404±7	11.8±0.7	32.5±0.1	8.052±0.007	0.45±0.12	12	8.5	0.35	0.19	0.01	0.3
2013/02	351±7	403±5	10.6±0.5	32.6±0.2	8.063±0.003	0.56±0.11	14	6.5	0.30	0.24	0.01	0.2
2013/03	351±7	403±7	10.6±0.5	32.7±0.4	8.059±0.010	n.m.	16	9.2	0.67	0.56	0.01	n.m.
2013/04	344±31	400±5	12.2±1.0	32.9±0.3	8.070±0.043	n.m.	26	7.7	0.80	0.32	0.04	n.m.
2013/05	233±29	394±6	17.8±2.2	31.4±0.9	8.163±0.099	n.m.	38	6.5	1.02	0.48	0.21	n.m.

n.m., not measured.
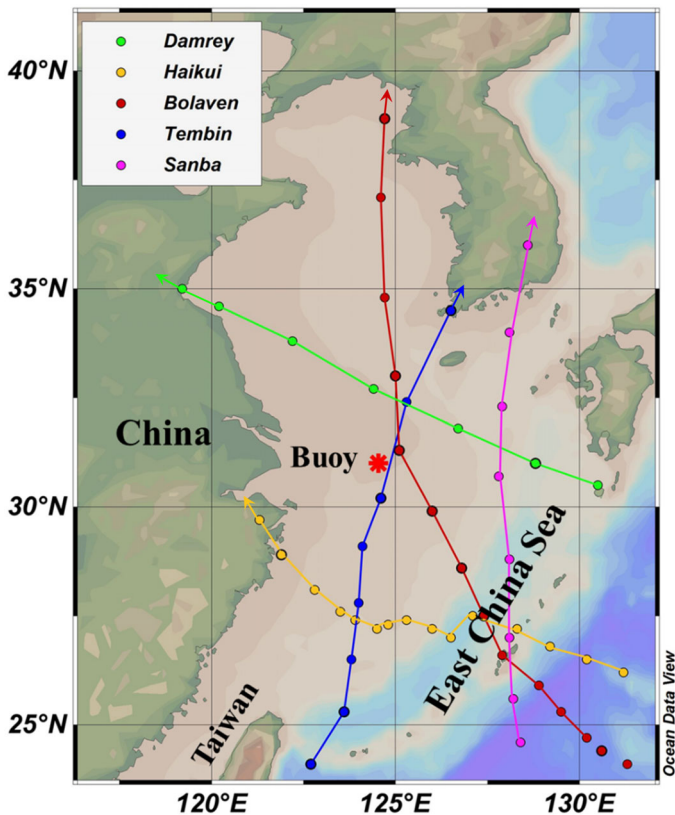
Fig. 3. Typhoon tracks along the East China Sea during summer and autumn of 2012. Green: *Damrey*, 28 July 2012–02 August 2012; Yellow: *Haikui*, 02–08 August 2012; Red: *Bolaven*, 20–28 August 2012; Blue: *Tembin*, 19–30 August 2012; Pink: *Sanba*, 10–17 September 2012. Data were from Unisys Weather (http://50.206.172.193/hurricane/w_pacific/2012H/index.php) showing the track of typhoon at 6-h intervals as dots. The red star denotes the buoy location, and arrows show the direction of typhoon.

comparable to that during *Damrey* with no obvious change in turbidity was found. This might suggest the limited impact of *Haikui* on the study site and therefore it will not be discussed further.. During the impact of *Damrey*, there was no clear evidence of deep mixing as temperature and salinity seemed to only have some random covariations (Fig. 4c). The increase in turbidity was accompanied by a sharp increase in Chl *a* as large as 16 μg L^{-1} within 6 h. Sea surface pCO_2 was undersaturated from 01 to 03 August, while it became slightly oversaturated during the post-typhoon period (Fig. 4e).

Bolaven and *Tembin* came by the study site one after another within 4 d. Pressure decreased by 4 kPa and 2 kPa during their occurrences, with an increase in turbidity up to 9 NTU and 5 NTU, respectively. Both pressure and wind velocity reached their extreme values when these two typhoons were closest to the buoy. During *Bolaven* (27–29 August), temperature decreased along with increases in salinity, pCO_2 (Fig. 5c,e), and temperature-normalized pCO_2 (NpCO_2, not shown). The largest response in temperature was about −3.0°C, occurring 6 h after the pressure minimum, during which sea surface pCO_2 and NpCO_2 increased rapidly by 200 μatm and 242 μatm, respectively. The associated variations in temperature (decreased by 3.0°C), salinity (increased by 2.0), pH (decreased by 0.22), and turbidity (increased by 9 NTU, indicating bottom sediment resuspension), along with the increase in NpCO_2, suggested strong vertical mixing driven by the intense winds, which entrained the CO_2-rich deep water (Chou et al. 2009*b*) into the surface layer. During *Tembin* (29–31 August), the responses of these parameters were also conspicuous although the variations were much weaker (Fig. 5). An increasing trend in temperature was also observed: the largest amplitudes for variations in $pCO_{2,sw}$, pH, and temperature were 57 μatm, −0.06, and 2.1°C, respectively.
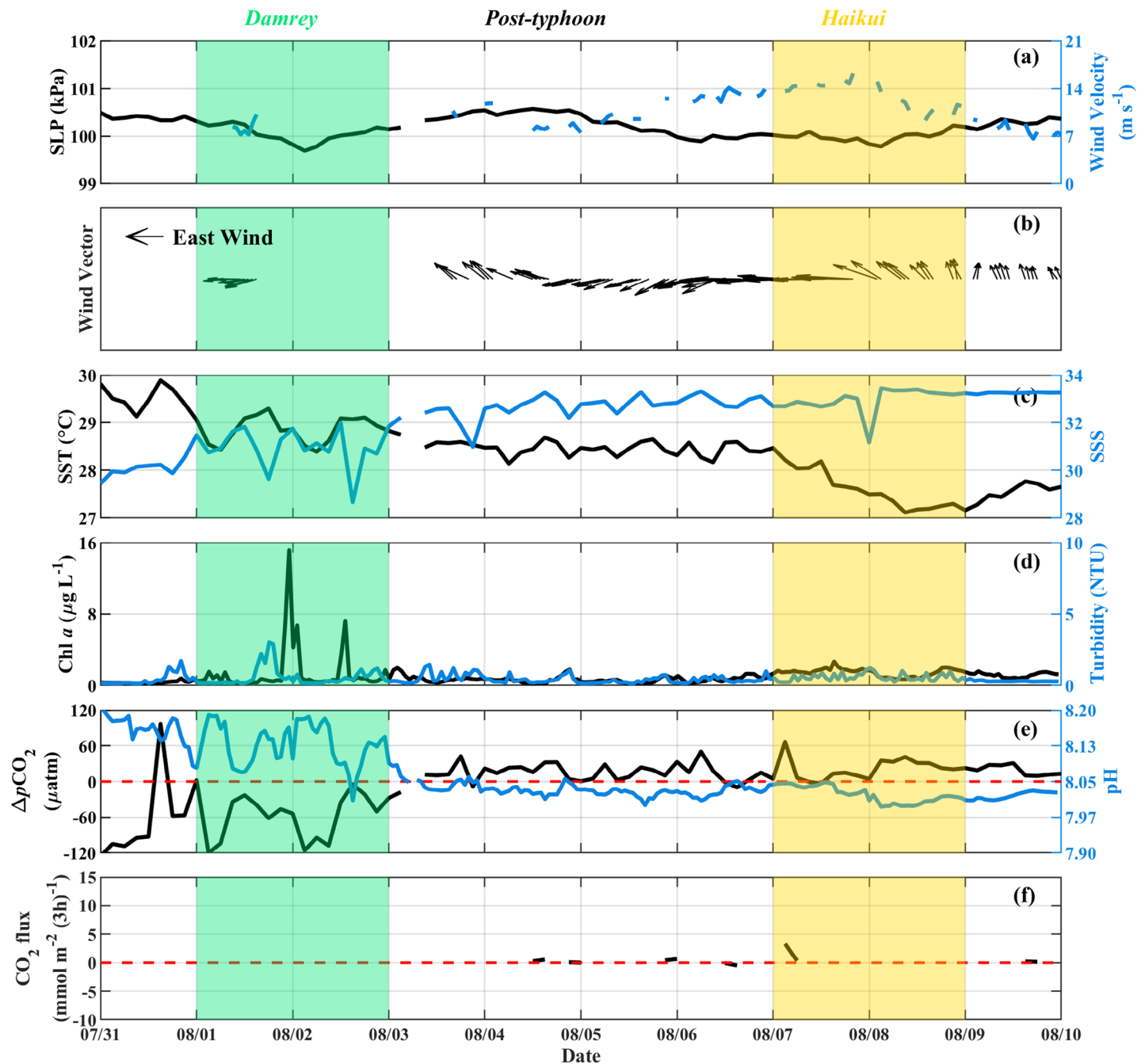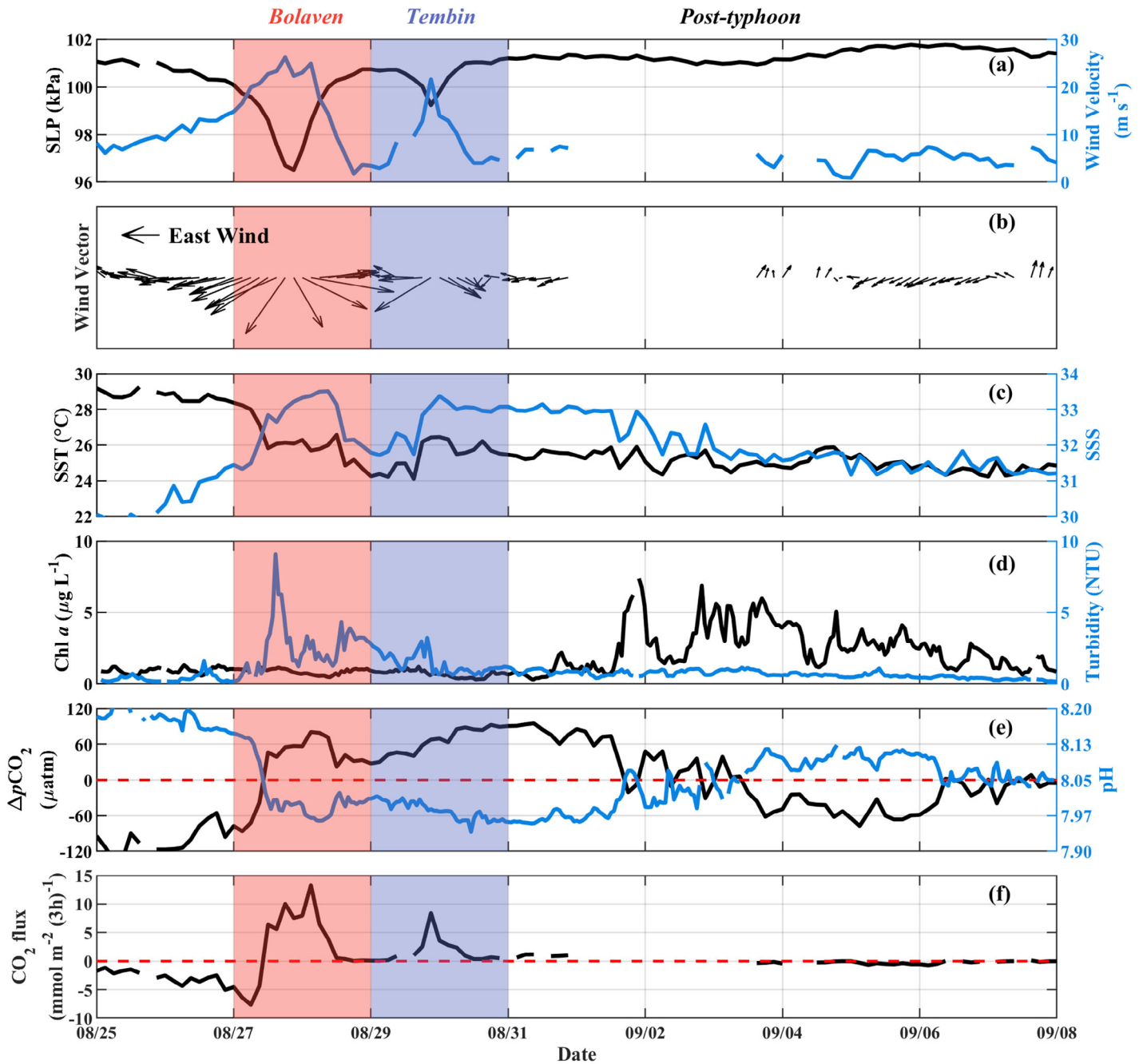
Fig. 4. Influence of typhoons Damrey and Haikui on ΔpCO$_2$ and other related parameters (**a:** SLP and wind velocity, **b:** wind vector, **c:** SST and SSS, **d:** Chl *a* and Turbidity, **e:** ΔpCO$_2$ and pH, and **f:** air-sea CO$_2$ flux) measured at the buoy site. The green shading indicates the Damrey-influenced period, and the yellow shading indicates the Haikui-influenced period. ΔpCO$_2$, difference between pCO$_{2,sw}$ and pCO$_{2,air}$; SLP, sea level pressure; SSS, sea surface salinity; SST, sea surface temperature.

An increase in Chl *a* appeared 2 d after the passage of *Tembin*, lasting from 02 September to 07 September, corresponding to the decrease in pCO$_2$. Due to the fact that these two typhoons passed the study site with an overlap, we did not completely separate one from another and we combined them as one event in the following sections.

Sanba went by the study site parallelly to the track of *Tembin* but much further away. Despite that it had less impact on pressure (a drop by 1 kPa), temperature (no significant decrease was observed apart from the diurnal signal), and salinity (increased by 1.5), the wind velocity and turbidity stimulated by *Sanba* were comparable to those

Fig. 5. Influence of typhoons Bolaven and Tembin on $\Delta p\mathrm{CO}_2$ and other related parameters (**a:** SLP and wind velocity, **b:** wind vector, **c:** SST and SSS, **d:** Chl *a* and Turbidity, **e:** $\Delta p\mathrm{CO}_2$ and pH, and **f:** air-sea CO$_2$ flux) measured at the buoy site. The red shading indicates the Bolaven-influenced period, and the blue shading indicates the Tembin-influenced period. $\Delta p\mathrm{CO}_2$, difference between $p\mathrm{CO}_{2,\mathrm{sw}}$ and $p\mathrm{CO}_{2,\mathrm{air}}$; SLP, sea level pressure; SSS, sea surface salinity; SST, sea surface temperature.

during *Bolaven* and *Tembin*. Surface $p\mathrm{CO}_2$ increased by 120 μatm with the study site turning from neutral to a CO$_2$ source, and lasting for around 10 d until gradual increase in Chl *a* was observed.

Throughout the passages of these typhoons, the covariations in $p\mathrm{CO}_{2,\mathrm{sw}}$ and pH were strongly correlated, with the

Pearson correlation coefficient of -0.99. In addition, we observed the changes in the wind vector field according to the movement of each individual typhoon (Figs. 5b, 6b): prior to the minimum pressure (indicating the closet approach of typhoon), it was usually east wind prevailed, whereas after the minimum pressure it was west wind prevailed.
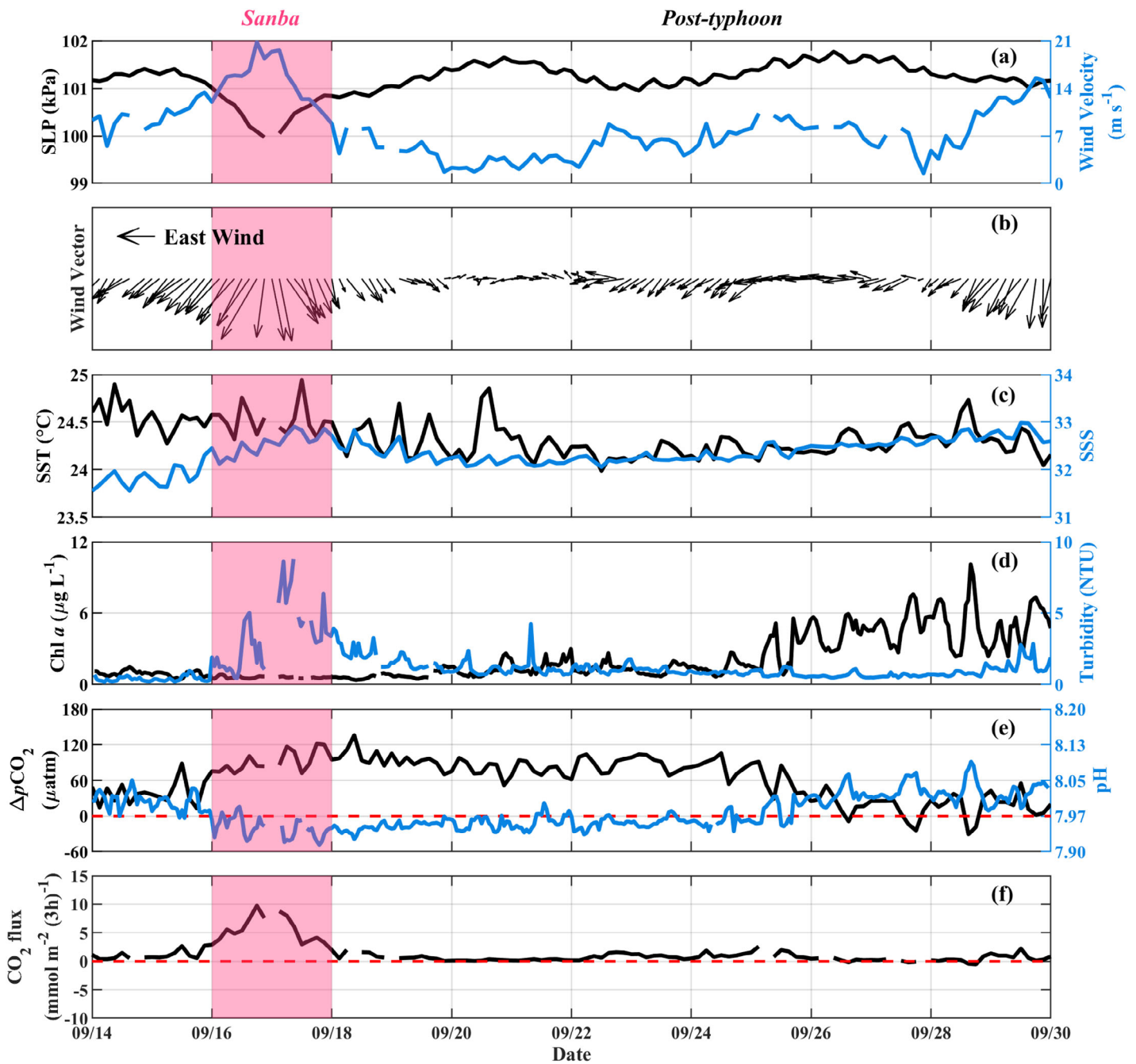
Fig. 6. Influence of typhoon Sanba on $\Delta p\mathrm{CO}_2$ and other related parameters (**a:** SLP and wind velocity, **b:** wind vector, **c:** SST and SSS, **d:** Chl *a* and Turbidity, **e:** $\Delta p\mathrm{CO}_2$ and pH, and **f:** air-sea CO_2 flux) measured at the buoy site. The pink shading indicates the Sanba-influenced period. $\Delta p\mathrm{CO}_2$, difference between $p\mathrm{CO}_{2,\mathrm{sw}}$ and $p\mathrm{CO}_{2,\mathrm{air}}$; SLP, sea level pressure; SSS, sea surface salinity; SST, sea surface temperature.

Discussion

Seasonal evolution of sea surface $p\mathrm{CO}_2$ and its controlling mechanisms

No conspicuous relationship between sea surface $p\mathrm{CO}_2$ and temperature at a yearly timescale was found during the observation. However, for some certain periods in late autumn and early winter, sea surface $p\mathrm{CO}_2$ followed the temperature-driven (thermodynamically expected) trend (gray curves in Fig. 7a). Data falling beyond the lower/upper limits (Fig. 7a) implied the nonthermal removal/addition of CO_2. The lower part in Fig. 7a (below the gray curves) consists of data mostly from the entire summer, and some from autumn and spring, respectively. The temperature-normalized $p\mathrm{CO}_2$ (N$p\mathrm{CO}_2$, Fig. 7b) values showed a positive relationship with salinity, with the lower end representing fresher Changjiang River plume and

upper end representing saltier subsurface water. In contrast, the upper part in Fig. 7a (above the gray curves) consists of data from mid-winter to early spring. The sea surface NpCO$_2$ exhibited a negative relationship with salinity, implying the mixing of different source of waters as discussed below.

From August to October, pCO$_{2,sw}$ was positively correlated with salinity (Pearson correlation coefficient of 0.73) and negatively correlated with temperature (Pearson correlation coefficient of −0.73). The low pCO$_{2,sw}$ along with low salinity and high temperature is attributed to the influence of the Changjiang River plume. Since the Changjiang River plume carries a large amount of organic carbon and nutrients, the upper estuary is usually supersaturated in CO$_2$ with respect to the atmosphere, whereas the mid and lower estuary is usually undersaturated in CO$_2$ due to the enhanced photosynthesis (Chen et al. 2012). On the contrary, the high pCO$_{2,sw}$ along with high salinity and low temperature is associated with the vertical mixing during typhoons, when CO$_2$-rich subsurface waters were entrained into the surface.

From October to the end of November (i.e., 02 October to 30 November), a continuous efflux of CO$_2$ was observed (Figs. 2c, 8a). During this period, salinity increased after the collapse of summer stratification (as described by Zhai and Dai 2009; see also Fig. 2b and Table 2 for the monthly variation in salinity), pCO$_{2,sw}$ reached its maximum value of 513 μatm on 24 October (sharp peak in Fig. 7a). Afterward, pCO$_{2,sw}$ gradually decreased and re-equilibrated with the atmosphere.

From December on, pCO$_{2,sw}$ was fairly constant and was lower than the atmospheric level (Fig. 2c). It decreased slightly along with the decreasing temperature (Fig. 7a). The ratio between the natural logarithm of pCO$_{2,sw}$ (ln$p$CO$_2$) and temperature ($\partial \ln p$CO$_2/\partial T$) was only 0.0096 °C^{-1}, much lower than the expected dependence (i.e., 0.0423°C^{-1}, Takahashi et al. 1993), suggesting that the existence of nonthermal processes affecting pCO$_{2,sw}$ partly counteracted the temperature effect. This is also supported by increasing NpCO$_2$ with decreasing salinity (Fig. 7b). Biological activity (e.g., respiration) seems implausible because it is limited by low temperatures in winter on the East China Sea shelf (Gong et al. 2003). Air–sea CO$_2$ exchange only contributes minorly (Li et al. 2018) because it requires a much longer timescale (from months to a year, Jones et al. 2014). Lateral mixing with Yellow Sea Water (lower salinity, lower temperature, and higher pCO$_2$ than East China Sea offshore water; Zhai et al. 2014) is therefore the most likely explanation for the increase in pCO$_2$ and NpCO$_2$. After the onset of spring bloom in May 2013, corresponding with the significant decrease in salinity (Fig. 7b) which was driven by the freshen Changjiang River plume input, pCO$_{2,sw}$ began to fluctuate again.

Air–sea CO$_2$ fluxes

The study site overall acted as a net CO$_2$ sink throughout the observation (−1.48 ± 7.16 mmol m^{-2} d^{-1}), however, with

significant temporal variability (Fig. 8). In summer, the study site served as a source of CO$_2$ to the atmosphere, with a seasonal average flux of 1.69 ± 10.26 mmol m^{-2} d^{-1}. This is contrary to the general consensus that the Changjiang plume is a CO$_2$ sink in summer due to the large nutrient inputs and subsequent biological CO$_2$ uptake (Chou et al. 2009a; Zhai and Dai 2009; Guo et al. 2015). There are three possible explanations for this discrepancy. First, it could be due to the lack of data in June and July, when the East China Sea shelf would generally absorb CO$_2$ from the atmosphere if not perturbed by typhoons, when the CO$_2$ influx could reach as high as −6.5 ± 10.7 mmol m^{-2} d^{-1} (Guo et al. 2015). Second, the influence of typhoon *Bolaven* and *Tembin* in August (*Damrey* was not taken into account due to the lack of wind velocity data) should have played a predominant role in shifting the direction of CO$_2$ flux. The CO$_2$ flux reached as high as 32 mmol m^{-2} d^{-1}, accompanied by a wind velocity of 25 m s^{-1}. The average CO$_2$ flux during typhoon period was 13.91 ± 10.92 mmol m^{-2} d^{-1}; whereas it was −0.79 ± 7.44 mmol m^{-2} d^{-1} in the absence of typhoon influence (Fig. 8b). It is therefore presumable to state that the study site could be a CO$_2$ sink if no severe weather events happened. Third, the study site was located at the edge of the most productive area, which resulted in a weaker CO$_2$ sink than the average of the Changjiang River plume (Guo et al. 2015).

In autumn, the CO$_2$ flux estimate was 4.59 ± 7.83 mmol m^{-2} d^{-1}, to some extent higher than previous estimates (Zhai and Dai 2009; Guo et al. 2015) even if the same gas transfer velocity parameterization (Wanninkhof 1992) was applied. Similar to summer, this difference was partly attributed to the passage of typhoon *Sanba* on 16–18 September, when the average CO$_2$ flux reached 31.01 ± 19.72 mmol m^{-2} d^{-1}. In addition, the collapse of summer stratification and the resulting CO$_2$ degassing also contributed to the enhanced CO$_2$ flux, as previously reported by Zhai and Dai (2009).

In winter and spring, the study site turned into a moderate CO$_2$ sink, with less temporal variability. The fluxes were −5.06 ± 3.50 mmol m^{-2} d^{-1} and −4.15 ± 3.35 mmol m^{-2} d^{-1} for the two seasons, respectively. These estimates were in reasonable agreement with previous studies (−5 to −14 mmol m^{-2} d^{-1} in winter by Guo et al. 2015, and Zhai and Dai 2009; −2 to −18 mmol m^{-2} d^{-1} in spring by Guo et al. 2015, and Zhai and Dai 2009 in the adjacent area) than those in summer and autumn which were characterized by large variability.

Impact of typhoon on pCO$_2$ and associated parameters

In general, we observed three evolutional stages during typhoons for those approaching the study site from the south (Fig. 9). At pre-typhoon stage (prior to colored shadings in Figs. 4–6; stage I in Fig. 9a), east wind prevailed as the typhoon getting toward the buoy since tropical depressions spin cyclonically in the northern hemisphere (Figs. 5b, 6b).
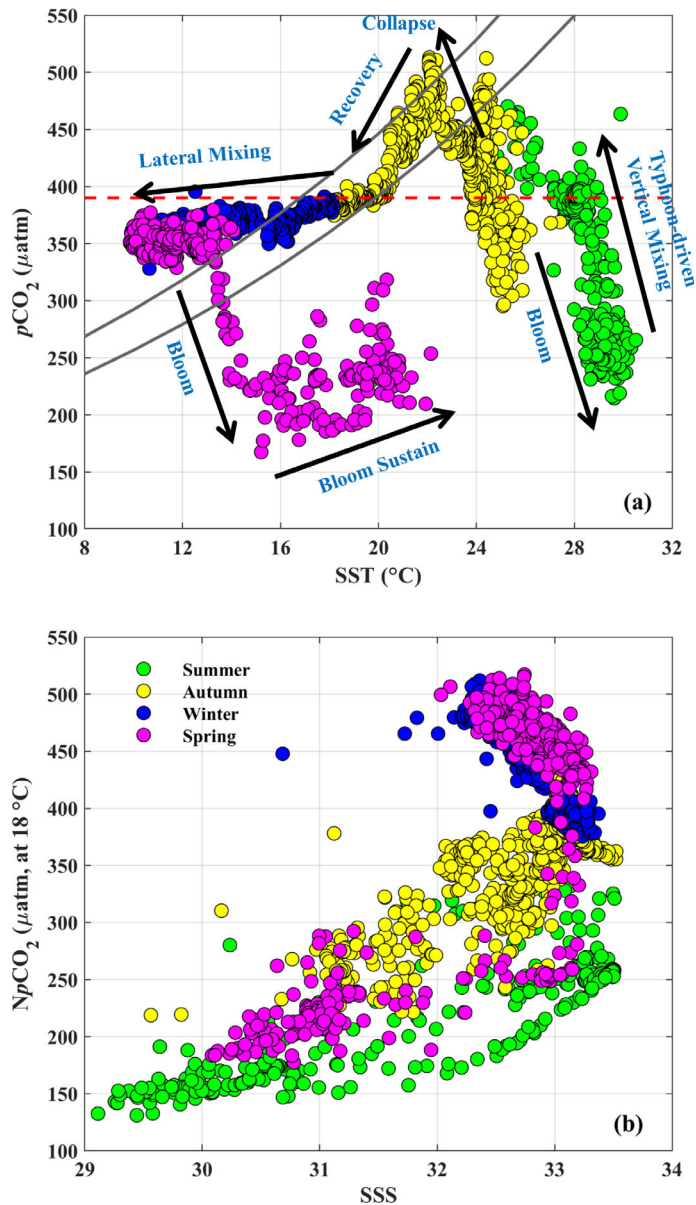
Fig. 7. Relationship between (**a**) sea surface pCO$_2$ and sea surface temperature (SST), and (**b**) sea surface temperature-normalized pCO$_2$ (NpCO$_2$) and sea surface salinity (SSS) at the buoy site. NpCO$_2$ in panel (**b**) was normalized to the average SST (18°C). The gray curves in panel (**a**) represent the thermodynamically expected pCO$_2$, with functions of $410 \times e^{0.0423 \times (SST-18)}$ and $360 \times e^{0.0423 \times (SST-18)}$ μatm, in which 410 and 360 μatm are the upper and lower ranges of the observed atmospheric pCO$_2$. The red dashed line is the average atmospheric pCO$_2$ level (390 μatm). Black arrows show the evolution of sea surface pCO$_2$, the slopes of which are indicative rather than quantitative.

Such east wind drives offshore water masses toward nearshore, which resulted in an increase in salinity from the very beginning of typhoon (prior to the colored shadings in Figs. 4c, 5c, 6c), and it was usually not necessarily accompanied by an increase in pCO$_2$ (e.g., Fig. 6c,e). For the observed typhoons (Figs. 4–6), the average salinity increase during this stage was

2.03. At the onset of typhoon (colored shadings in Figs. 5c, 6c; stage II in Fig. 9b), strong winds always stimulated vertical mixing and sediment resuspension and hence increased turbidity, and surface pCO$_2$ was therefore elevated (Figs. 5e, 6e). For the observed typhoons, the pCO$_{2,sw}$ increase during this stage reached as large as 187 μatm (*Bolaven* and *Tembin*) and 52 μatm (*Sanba*), respectively. At post-typhoon stage (following the colored shadings in Figs. 4–6; stage III in Fig. 9c), west wind prevailed after the passage of typhoon (Figs. 5b, 6b), which was capable of blowing the nearshore water eastward and offshore. In addition, the surface ocean condition would normally favor phytoplankton blooms in several days with the supply of nutrients from subsurface waters (Chen et al. 2017; Wang et al. 2017a,b). The pCO$_2$ would consequently go down as observed (Figs. 5d, 6d). For the observed typhoons, the pCO$_{2,sw}$ decrease during this stage reached as large as 166 μatm (*Bolaven* and *Tembin*) and 169 μatm (*Sanba*), respectively.

Figures 4–6 demonstrate, however, the different response in Chl a to typhoons during the observation. Generally, Chl a showed no evident changes during the first few days of typhoon, except *Damrey*, because strong turbulence under high winds do not favor phytoplankton blooms (Wang et al. 2017a,b). In the case of *Damrey* (Fig. 4), turbidity only increased by 3 NTU (no wind velocity data available) as the typhoon approaching the study site, suggesting the minor impact of *Damrey* on the observing system. Given that the large fluctuation in Chl a corresponded to the changes in temperature and salinity (Fig. 4c,d), we suggest that it was likely related to the cross-shelf export of coastal waters with extremely high Chl a. In the case of *Bolaven* and *Tembin* (Fig. 5), a sudden increase in Chl a started from 01 September, reaching up to 7 μg L^{-1}. Chl a then gradually decayed and persisted for around 1 week, coinciding with the decreases in salinity and pCO$_{2,sw}$. In contrast, in the case of *Sanba* (Fig. 6), surprisingly, a slight increasing trend in salinity (by 0.5) was found to accompany the gradual increase in Chl a which started from 25 September, with the highest Chl a concentration reaching 10 μg L^{-1}. Despite the different response in Chl a, ΔpCO$_2$ has overall the similar natures: the study site was turned into a CO$_2$ source during typhoon due to the strong vertical mixing indicated by the elevation in turbidity (stage II in Fig. 9) but recovered following phytoplankton blooms (stage III in Fig. 9).

The above phenomenon reveals two different mechanisms controlling the variation of pCO$_2$ at stage III. For *Bolaven* and *Tembin*, we suggest that the increase in Chl a and recovery of pCO$_{2,sw}$ were caused by the movement of the Changjiang River plume (low salinity, low pCO$_{2,sw}$ but productive) induced by wind (i.e., west wind) because salinity was observed to decrease. Chl a also evolved from thriving to decayed. This could happen immediately after the passage of typhoon, therefore the time lag in responses of Chl a and salinity was only 2 d. For *Sanba*, we suggest that the increase
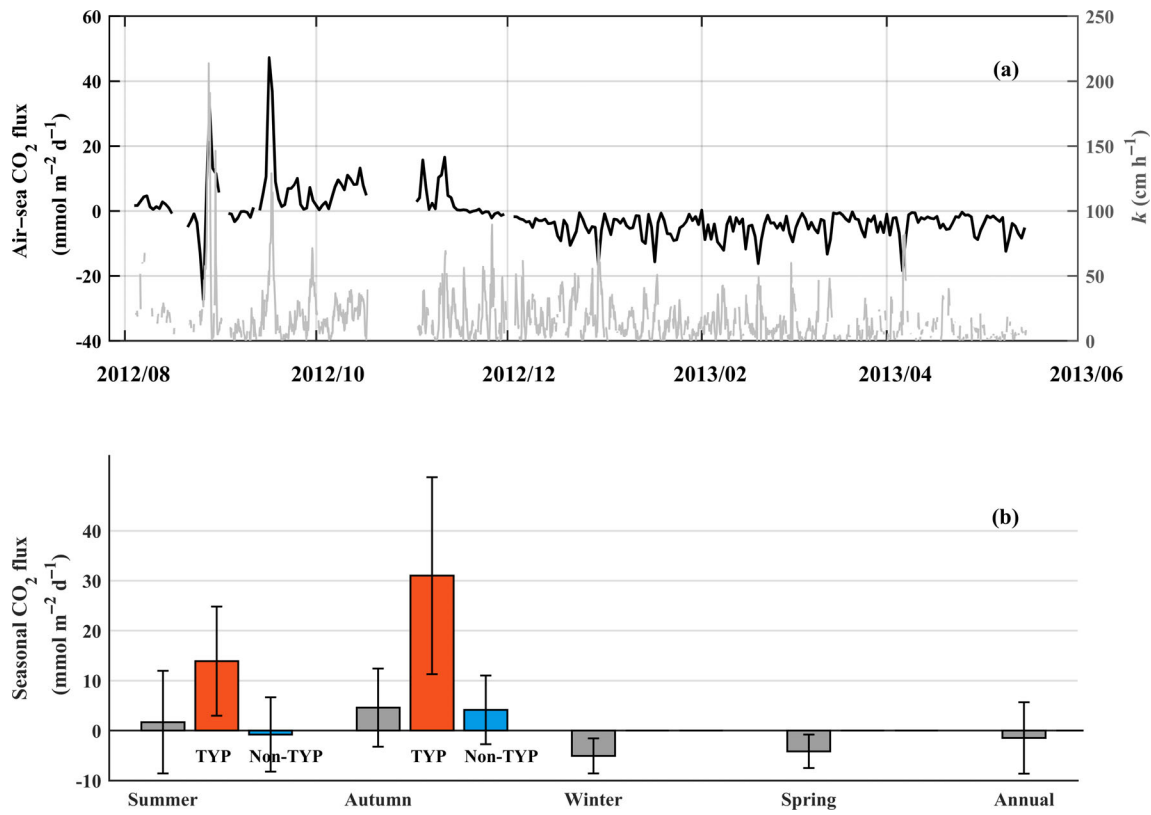
Fig. 8. Air–sea CO$_2$ fluxes at the study site. (**a**) Time series of CO$_2$ fluxes and gas transfer velocities (*k*); (**b**) Seasonal CO$_2$ fluxes. The CO$_2$ fluxes in panel (**b**) are expressed as average ± standard deviation. Periods subjected to typhoon influence (i.e., 27–31 August in summer and 16–18 September in autumn) are specified by "TYP," otherwise specified by "Non-TYP."

in Chl *a* and recovery of *p*CO$_{2,sw}$ were due to in situ growth of phytoplankton because salinity increase was observed since 22 September (although salinity dropped slightly during 18–22 September with insignificant change in Chl *a*). Chl *a* also evolved from negligible to thriving. Therefore, although Chl *a* and CO$_2$ drawdown were eventually found in these typhoons, they were, however, experiencing different processes. As most previous studies only focused on the biogeochemical response of *p*CO$_{2,sw}$ to typhoon due to the latter process (e.g., Hung and Gong 2011; Lin 2012), our study shows the possibility of typhoon-induced movement of water masses which has not previously been appreciated. This finding also emphasizes the more complex and wider impact of typhoon on CO$_2$ chemistry in coastal seas with large spatial variability than in the open ocean.

Impact of typhoons on air–sea CO$_2$ fluxes

We examined the contributions of different factors that influenced the temporal variability of air–sea CO$_2$ flux during typhoons based on Eq. 6. The first term on the right-hand side of Eq. 6 is a function of wind velocity square (Eq. 4), therefore wind velocity exerts the greatest impact on the gas transfer coefficient term.

Figure 10 shows the contributions of different terms. We do not consider the influence of *Damrey* and *Haikui* due to the lack of wind velocity data, and we combine *Bolaven* and *Tembin* given the short interval between them. For both events (i.e., *Bolaven & Tembin* and *Sanba*), *p*CO$_{2,air}$ generally played a negligible role throughout the observation. Prior to the pressure minima (indicating the closet approach of typhoon), the increase in CO$_2$ efflux was due to the combination of increase in wind velocity and supply of CO$_2$-rich subsurface water; after the pressure minima, the decrease in CO$_2$ efflux was dominated by the decreasing wind velocity, expect for some certain periods during *Sanba*, when the diurnal signal of increasing *p*CO$_{2,sw}$ (corresponding to semidiurnal tide-driven variations) seemed to compete with wind velocity (Fig. 10b). Specifically, the temporal variability in CO$_2$ flux before pressure minimum during *Sanba* was more complex than that during *Bolaven & Tembin*. Unlike the monotonically increasing trend in wind velocity, *p*CO$_{2,sw}$ exhibited more pronounced diurnal cycle, as indicated by the abrupt peaks and declines (Fig. 10b). As a result, the contributions from wind velocity and *p*CO$_{2,sw}$ tended to offset when their variations were at negative phase due to diurnal variations or decrease in *p*CO$_{2,sw}$ with lower temperature; whereas tended to accumulate at positive phase.
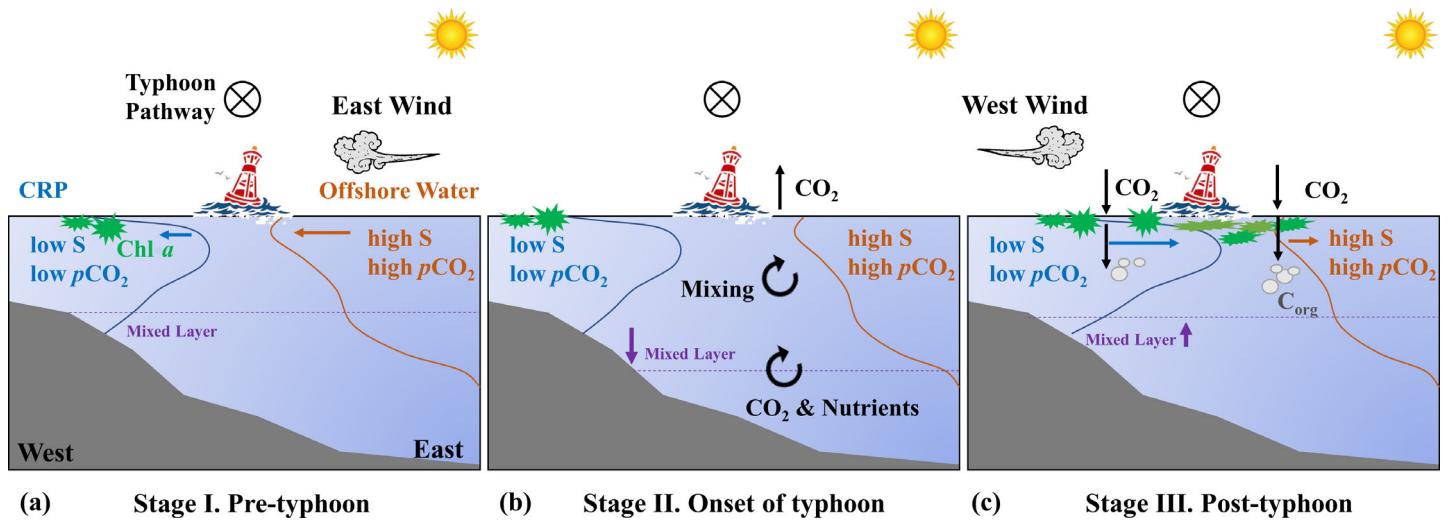
Fig. 9. Dynamics of wind and surface ocean during three stages of typhoon (**a**: pre-typhoon, **b**: onset of typhoon, and **c**: post-typhoon) at the buoy site. Circled cross denotes the direction (into the page) of typhoon pathway. Green shapes represent phytoplankton and Chl *a*, grey circles represent bio-logical-sequestered organic carbon (Corg). Stage I: east wind prevails and drives the westward movement of offshore surface water; Stage II: strong wind promotes vertical mixing and hence CO_2 outgassing; Stage III: west wind prevails and drives the eastward movement of Changjiang River plume (CRP), meanwhile, the reinvigoration of primary production drawdowns CO_2 from the atmosphere. Capitalized "S" represents salinity. This schematic is a simplified representation of the evolution of surface ocean illustrated more completely in main text.

The air–sea CO_2 flux in both summer and autumn was influenced significantly by the passage of typhoons. In summer with no perturbation from typhoons, the study site was a weak sink (with average air–sea CO_2 flux of -0.79 ± 7.44 mmol m^{-2} d^{-1}). However, the study site was converted to a strong CO_2 source of 13.91 ± 10.92 mmol m^{-2} d^{-1} by typhoon, the strength of which was $\sim$ 18-folds of the CO_2 sink in the periods without typhoon. Therefore, although the period of typhoon perturbation was short ($\sim$ 4 d), typhoons completely dominated the seasonal CO_2 sink/source status. In summer, the study site accumulatively absorbed 42 mmol m^{-2} CO_2 in the absence of typhoon (we have only 1-month data in summer, therefore this magnitude is small). However, *Bolaven* (27—29 August) and *Tembin* (29–31 August) contributed 52 mmol m^{-2} and 30 mmol m^{-2} CO_2 release, respectively, ending up with the accumulative flux of 41 mmol m^{-2} CO_2 into the atmosphere in summer. The amount of CO_2 emitted from the sea surface during typhoon was twice as much as the CO_2 uptake at the other time in summer. In autumn with no perturbation from typhoons, the study site was a moderate CO_2 source of 4.14 mmol m^{-2} d^{-1}. The CO_2 source was enhanced by $\sim$ 8-folds to be 31.01 ± 19.72 mmol m^{-2} d^{-1} during the passage of typhoon *Sanba*. The study site accumulatively released 242 mmol m^{-2} of CO_2 to the atmosphere, mostly attributed to the collapse of summer stratification. Although typhoon *Sanba* perturbation was only 2 d, it additionally contributed 93 mmol m^{-2} CO_2 emission, accounting for 28% of the total CO_2 emission in autumn.

Despite the fact that blooms drawdown pCO_2 by a large amount (around 100 μatm) at post-typhoon stage (Figs. 5d,

6d), it was not strengthening the CO_2 sink (due to low wind velocity; Figs. 5f, 6f) but just accelerating the re-equilibration/recovery of pCO_2. Therefore, we emphasize that the typhoon-induced CO_2 emission and its potential in shifting the CO_2 sink-source status has an irreversible impact on air–sea CO_2 flux, especially for such river-dominated margin system. We also argue that the previous understanding of sea surface CO_2 chemistry and air–sea CO_2 flux in summer and autumn based on shipboard observations (e.g., Guo et al. 2015) might need revision to take into account of the typhoon impact.

Concluding remarks

Time-series observation of sea surface pCO_2 and pH data, along with other related parameters, were obtained from July 2012 to June 2013 with an autonomous buoy monitoring system deployed on the East China Sea shelf. On annual scale, the study site was overall a CO_2 sink with respect to the atmosphere. On seasonal time scale, the study site was a CO_2 source in summer and autumn due to the mixing of CO_2-rich subsurface water, while it converted to a CO_2 sink in winter and spring mainly due to low temperature in winter and strong biological CO_2 uptake in spring. The passages of typhoon exerted significant influence on sea surface pCO_2, pH, and air–sea CO_2 flux. In summer, typhoons converted the study site from CO_2 sink to source although the average sea surface pCO_2 was below the atmospheric level; in autumn, the typhoon strengthened the CO_2 source by a quarter. We have suggested a novel concept of three different stages of the northward movement of typhoon involving wind-induced
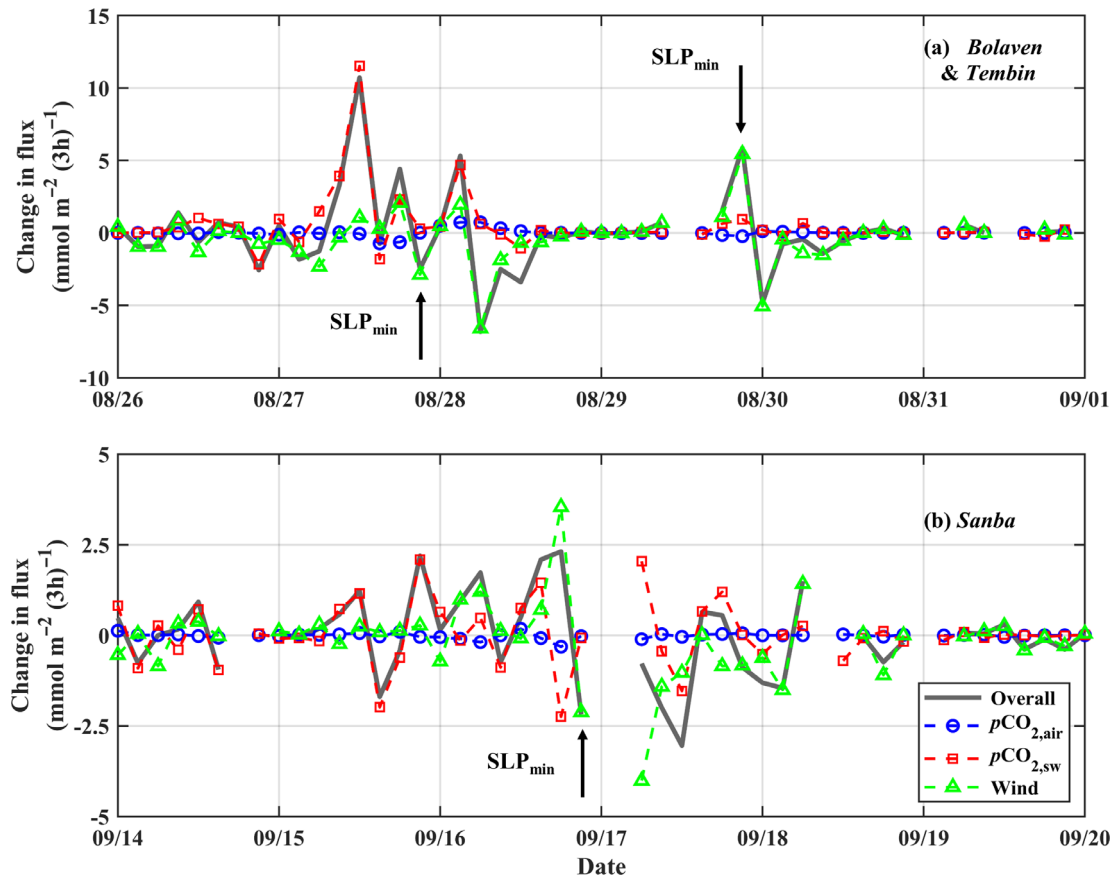
Fig. 10. Contributions of pCO$_{2,air}$ (blue circle), pCO$_{2,sw}$ (red square), and wind velocity (green triangle) to the change in CO$_2$ flux (gray solid line) during typhoons: (**a**) *Bolaven* and *Tembin*, (**b**) *Sanba*. Arrows show the timing of the sea level pressure (SLP) minima for each typhoon.

biogeochemical response of surface pCO$_2$. The lateral surface seawater movement was significant during pre- and post-typhoon periods when east and west wind prevailed, respectively, and vertical mixing was significant at the onset of typhoon. The variation of wind field (direction) were of great importance in elevating salinity prior to typhoon, as well as in triggering the rapid growth of Chl a along with decreasing pCO$_2$ after the passage of typhoon. Given the great impact of typhoon on air–sea CO$_2$ exchange, we suggested the necessity of considering typhoon impact the synthesized studies, especially for marginal seas, which are subjected to large spatial variability.

References

Bai, Y., and others. 2014. Summertime Changjiang River plume variation during 1998–2010. Journal of Geophysical Research: Oceans 119: 6238–6257. doi:10.1002/2014JC009866

Bates, N., and others. 2014. A time-series view of changing ocean chemistry due to ocean uptake of anthropogenic CO$_2$ and ocean acidification. Oceanography **27**: 126–141. doi:10.5670/oceanog.2014.16

Bates, N. R., T. Takahashi, D. W. Chipman, and A. H. Knap. 1998. Variability of pCO2 on diel to seasonal timescales in the Sargasso Sea near Bermuda. Journal of Geophysical Research: Oceans **103**: (C8) 15567–15585. http://dx.doi.org/10.1029/98jc00247

Bauer, J. E., W.-J. Cai, P. A. Raymond, T. S. Bianchi, C. S. Hopkinson, P. A. G. Regnier. 2013. The changing carbon cycle of the coastal ocean. Nature **504**: (7478) 61–70. http://dx.doi.org/10.1038/nature12857

Bond, N. A., and others. 2011. Upper ocean response to Typhoon Choi-Wan as measured by the Kuroshio Extension Observatory mooring. Journal of Geophysical Research: Oceans **116**: C02031. doi:10.1029/2010JC006548

Bozec, Y., and others. 2011. Diurnal to inter-annual dynamics of pCO$_2$ recorded by a CARIOCA sensor in a temperate coastal ecosystem (2003–2009). Mar. Chem. **126**: 13–26. doi: 10.1016/j.marchem.2011.03.003

Cai, W.-J. 2011. Estuarine and coastal ocean carbon paradox: CO$_2$ sinks or sites of terrestrial carbon incineration? Ann.

Rev. Mar. Sci. **3**: 123–145. doi:10.1146/annurev-marine-120709-142723

Cai, W.-J., and others. 2004. The biogeochemistry of inorganic carbon and nutrients in the Pearl River Estuary and the adjacent northern South China Sea. Cont. Shelf Res. **24**: 1301–1319. doi: 10.1016/j.csr.2004.04.005

Chen, C.-T. A. 2009. Chemical and physical fronts in the Bohai, Yellow and East China Seas. J. Mar. Syst. **78**: 394–410. doi:10.1016/j.jmarsys.2008.11.016

Chen, C.-T. A., and S.-L. Wang. 1999. Carbon, alkalinity and nutrient budgets on the East China Sea continental shelf. J. Geophys. Res. Oceans **104**: 20675–20686. doi: 10.1029/1999jc900055

Chen, C.-T. A., and A. V. Borges. 2009. Reconciling opposing views on carbon cycling in the coastal ocean: Continental shelves as sinks and near-shore ecosystems as sources of atmospheric CO_2. Deep-Sea Res. Part II Top. Stud. Oceanogr. **56**: 578–590. doi: 10.1016/j.dsr2.2009.01.001

Chen, C.-T. A., T.-H. Huang, Y.-H. Fu, Y. Bai, and X. He. 2012. Strong sources of CO_2 in upper estuaries become sinks of CO_2 in large river plumes. Curr. Opin. Environ. Sustain. **4**: 179–185. doi: 10.1016/j.cosust.2012.02.003

Chen, D., L. He, F. Liu, and K. Yin. 2017. Effects of typhoon events on chlorophyll and carbon fixation in different regions of the East China Sea. Estuar. Coast. Shelf Sci. **194**: 229–239. doi:10.1016/j.ecss.2017.06.026

Chou, W.-C., G.-C. Gong, D. D. Sheu, C.-C. Hung, and T.-F. Tseng. 2009*a*. Surface distributions of carbon chemistry parameters in the East China Sea in summer 2007. J. Geophys. Res. Oceans **114**: C07026. doi:10.1029/2008JC005128

Chou, W. C., G. C. Gong, D. D. Sheu, S. Jan, C. C. Hung, and C. C. Chen. 2009*b*. Reconciling the paradox that the heterotrophic waters of the East China Sea shelf act as a significant CO_2 sink during the summertime: Evidence and implications. Geophys. Res. Lett. **36**: L15607. doi:10.1029/2009GL038475

Chou, W.-C., P. Y. Tishchenko, K.-Y. Chuang, G.-C. Gong, E. M. Shkirnikova, and P. P. Tishchenko. 2017. The contrasting behaviors of CO_2 systems in river-dominated and ocean-dominated continental shelves: A case study in the East China Sea and the Peter the Great Bay of the Japan/East Sea in summer 2014. Mar. Chem. **195**: 50–60. doi:10.1016/j.marchem.2017.04.005

D'Asaro, E. A., and others. 2011. Typhoon-ocean interaction in the western North Pacific: Part 1. Oceanography **24**: 24–31. doi:10.5670/oceanog.2011.91

Dai, A., and K. E. Trenberth. 2002. Estimates of freshwater discharge from continents: Latitudinal and seasonal variations. *Journal of Hydrometeorology* **3**: 660-687. doi:10.1175/1525-7541(2002)003<0660:eofdfc>2.0.co;2

Dai, M., Z. Lu, W. Zhai, B. Chen, Z. Cao, K. Zhou, W. J. Cai, and C. T. A. Chenc. 2009. Diurnal variations of surface seawater pCO_2 in contrasting coastal environments. Limnol. Oceanogr. **54**: 735–745. doi: 10.4319/lo.2009.54.3.0735

Dai, M., and others. 2013. Why are some marginal seas sources of atmospheric CO_2? Geophys. Res. Lett. **40**: 2154–2158. doi: 10.1002/grl.50390

Dickson, A. G. 1990. Standard potential of the reaction: AgCl (s)+ 12H₂ (g) = Ag (s)+ HCl (aq), and and the standard acidity constant of the ion HSO₄⁻ in synthetic sea water from 273.15 to 318.15 K. J. Chem. Thermodyn. **22**: 113–127. doi: 10.1016/0021-9614(90)90074-z

Dickson, A. G., and F. J. Millero. 1987. A comparison of the equilibrium constants for the dissociation of carbonic acid in seawater media. Deep-Sea Res. A **34**: 1733–1743. doi: 10.1016/0198-0254(88)92460-0

Gong, G.-C., Y.-H. Wen, B.-W. Wang, and G.-J. Liu. 2003. Seasonal variation of chlorophyll-*a* concentration, primary production and environmental conditions in the subtropical East China Sea. Deep-Sea Res. Part II Top. Stud. Oceanogr. **50**: 1219–1236. doi: 10.1016/s0967-0645(03)00019-5

Gruber, N. 2015. Ocean biogeochemistry: Carbon at the coastal interface. Nature **517**: 148–149. doi:10.1038/nature14082

Guo, X. H., W. D. Zhai, M. H. Dai, C. Zhang, Y. Bai, Y. Xu, Q. Li, and G. Z. Wang. 2015. Air–sea CO_2 fluxes in the East China Sea based on multiple-year underway observations. Biogeosciences **12**: 5495–5514. doi:10.5194/bg-12-5495-2015

Hofmann, G. E., and others. 2011. High-frequency dynamics of ocean pH: A multi-ecosystem comparison. PLoS One **6**: e28983. doi:10.1371/journal.pone.0028983

Hung, C.-C., and G.-C. Gong. 2011. Biogeochemical responses in the southern East China Sea after typhoons. Oceanography 24: 42–51. doi:10.5670/oceanog.2011.93

Hung, J.-J., C.-H. Chen, G.-C. Gong, D.-D. Sheu, and F.-K. Shiah. 2003. Distributions, stoichiometric patterns and cross-shelf exports of dissolved organic matter in the East China Sea. Deep Sea Research Part II: Topical Studies in Oceanography 50: 1127–1145. doi:10.1016/s0967-0645(03)00014-6

Jones, D. C., T. Ito, Y. Takano, and W.-C. Hsu. 2014. Spatial and seasonal variability of the air-sea equilibration timescale of carbon dioxide. Global Biogeochem. Cycles **28**: 1163–1178. doi:10.1002/2014GB004813

Laruelle, G. G., R. Lauerwald, B. Pfeil, and P. Regnier. 2014. Regionalized global budget of the CO_2 exchange at the air-water interface in continental shelf seas. Global Biogeochem. Cycles **28**: 1199–1214.

Lee, K., T.-W. Kim, R. H. Byrne, F. J. Millero, R. A. Feely, and Y.-M. Liu. 2010. The universal ratio of boron to chlorinity for the North Pacific and North Atlantic oceans. Geochim. Cosmochim. Acta **74**: 1801–1811. doi:10.1016/j.gca.2009.12.027

Lee, H.-J., and S.-Y. Chao. 2003. A climatological description of circulation in and around the East China Sea. Deep Sea

Research Part II: Topical Studies in Oceanography 50: 1065–1084. doi: 10.1016/S0967-0645(03)00010-9

Li, D., J. Chen, X. Ni, K. Wang, D. Zeng, B. Wang, H. Jin, D. Huang, and W.-J. Cai. 2018. Effects of biological production and vertical mixing on sea surface pCO_2 variations in the Changjiang River Plume during early autumn: A buoy-based time series study. J. Geophys. Res. Oceans **123**: 6156–6173. doi:10.1029/2017JC013740

Lin, I. I. 2012. Typhoon-induced phytoplankton blooms and primary productivity increase in the western North Pacific subtropical ocean. J. Geophys. Res. Oceans **117**: C03039. doi:10.1029/2011JC007626

Lin, I. I. 2012. Typhoon-induced phytoplankton blooms and primary productivity increase in the western North Pacific subtropical ocean. Journal of Geophysical Research: Oceans 117: C03039. doi:10.1029/2011JC007626

Liu, Q., X. Dong, J. Chen, X. Guo, Z. Zhang, Y. Xu, N. Huang, and M. Dai. 2019. Diurnal to interannual variability of sea surface pCO_2 and its controls in a turbid tidal-driven near-shore system in the vicinity of the East China Sea based on buoy observations. Mar. Chem. **216**: 103690. doi:10.1016/j.marchem.2019.103690

Martz, T. R., J. G. Connery, and K. S. Johnson. 2010. Testing the Honeywell Durafet® for seawater pH applications. Limnol. Oceanogr.: Methods **8**: 172–184. doi: 10.4319/lom.2010.8.172

Mehrbach, C. 1973. Measurement of the apparent dissociation constants of carbonic acid in seawater at atmospheric pressure. Limnol. Oceanogr. **18**: 897–907. doi: 10.4319/lo.1973.18.6.0897

Nemoto, K., T. Midorikawa, A. Wada, K. Ogawa, S. Takatani, H. Kimoto, M. Ishii, and H. Inoue. 2009. Continuous observations of atmospheric and oceanic CO_2 using a moored buoy in the East China Sea: Variations during the passage of typhoons. Deep-Sea Res. Part II Top. Stud. Oceanogr. **56**: 542–553. doi: 10.1016/j.dsr2.2008.12.015

Pierrot, D., E. Lewis, and D. Wallace. 2006. MS Excel program developed for CO_2 system calculations. ORNL/CDIAC-105a. Carbon Dioxide Information Analysis Center, Oak Ridge National Laboratory, US Department of Energy.

Price, J. F. 1981. Upper ocean response to a hurricane. Journal of Physical Oceanography 11: 153-175. doi: 10.1575/1912/10271

Sun, Q., D. Tang, L. Legendre, and P. Shi. 2014. Enhanced sea-air CO2 exchange influenced by a tropical depression in the South China Sea. Journal of Geophysical Research: Oceans 119: 6792–6804. doi:10.1002/2014JC010131

Sutton, A. J., R. A. Feely, C. L. Sabine, M. J. Mcphaden, T. Takahashi, F. P. Chavez, G. E. Friederich, and J. T. Mathis. 2014*a*. Natural variability and anthropogenic change in equatorial Pacific surface ocean pCO_2 and pH. Global Biogeochem. Cycles **28**: 131–145. doi:10.1002/2013GB004679

Sutton, A. J., and others. 2014*b*. A high-frequency atmospheric and seawater pCO_2 data set from 14 open-ocean sites using a moored autonomous system. Earth Syst. Sci. Data **6**: 353–366. doi:10.5194/essd-6-353-2014

Sweeney, C., E. Gloor, A. R. Jacobson, R. M. Key, G. Mckinley, J. L. Sarmiento, and R. Wanninkhof. 2007. Constraining global air-sea gas exchange for CO_2 with recent bomb ¹⁴C measurements. Global Biogeochem. Cycles **21**: GB2015. doi:10.1029/2006GB002784

Takahashi, T., J. Olafsson, J. G. Goddard, D. W. Chipman, and S. Sutherland. 1993. Seasonal variation of CO_2 and nutrients in the high-latitude surface oceans: A comparative study. Global Biogeochem. Cycles **7**: 843–878. doi: 10.1029/93GB02263

Tseng, C.-M., K. K. Liu, G. C. Gong, P. Y. Shen, and W. J. Cai. 2011. CO_2 uptake in the East China Sea relying on Changjiang runoff is prone to change. Geophys. Res. Lett. **38**: L24609. doi:10.1029/2011GL049774

Wada, A., T. Midorikawa, M. Ishii, and T. Motoi. 2011. Carbon system changes in the East China Sea induced by typhoons Tina and Winnie in 1997. Journal of Geophysical Research: Oceans 116: C07014. doi:10.1029/2010JC006701

Wang, K., and others. 2017*a*. Real-time monitoring of nutrients in the Changjiang Estuary reveals short-term nutrient-algal bloom dynamics. J. Geophys. Res. Oceans **122**: 5390–5403. doi:10.1002/2016JC012450

Wang, T., G. Liu, L. Gao, L. Zhu, and D. Li. 2017*b*. Biological responses to nine powerful typhoons in the East China Sea. Reg. Environ. Change **17**: 465–476. doi:10.1007/s10113-016-1025-0

Wanninkhof, R. 1992. Relationship between wind speed and gas exchange over the ocean. J. Geophys. Res. Oceans **97**: 7373–7382. doi: 10.1029/92jc00188

Weiss, R. F. 1974. Carbon dioxide in water and seawater: The solubility of a non-ideal gas. Mar. Chem. **2**: 203–215. doi: 10.1016/0304-4203(74)90015-2

Weiss, R. F., and B. A. Price. 1980. Nitrous oxide solubility in water and seawater. Mar. Chem. **8**: 347–359. doi:10.1016/0304-4203(80)90024-9

Xue, L., W.-J. Cai, X. Hu, C. Sabine, S. Jones, A. J. Sutton, L.-Q. Jiang, and J. J. Reimer. 2016. Sea surface carbon dioxide at the Georgia time series site (2006–2007): Air–sea flux and controlling processes. Prog. Oceanogr. **140**: 14–26. doi:10.1016/j.pocean.2015.09.008

Ye, H., Y. Sui, D. Tang, and Y. Afanasyev. 2013. A subsurface chlorophyll a bloom induced by typhoon in the South China Sea. J. Mar. Syst. **128**: 138–145. doi:10.1016/j.jmarsys.2013.04.010

Zhai, W., M. Dai, W.-J. Cai, Y. Wang, and Z. Wang. 2005. High partial pressure of CO_2 and its maintaining mechanism in a subtropical estuary: The Pearl River estuary, China. Mar. Chem. **93**: 21–32. doi:10.1016/j.marchem.2004.07.003

Zhai, W., M. Dai, and X. Guo. 2007. Carbonate system and CO₂ degassing fluxes in the inner estuary of Changjiang (Yangtze) River, China. Mar. Chem. **107**: 342–356. doi: 10. 1016/j.marchem.2007.02.011

Zhai, W., and M. Dai. 2009. On the seasonal variation of air–sea CO₂ fluxes in the outer Changjiang (Yangtze River) Estuary, East China Sea. Mar. Chem. **117**: 2–10. doi: 10. 1016/j.marchem.2009.02.008

Zhai, W.-D., J.-F. Chen, H.-Y. Jin, H.-L. Li, J.-W. Liu, X.-Q. He, and Y. Bai. 2014. Spring carbonate chemistry dynamics of surface waters in the northern East China Sea: Water mixing, biological uptake of CO₂, and chemical buffering capacity. J. Geophys. Res. Oceans **119**: 5638–5653. doi:10. 1002/2014JC009856

Zhai, W. D. and M. H. Dai, 2009. On the seasonal variation of air-sea CO2 fluxes in the outer Changjiang (Yangtze River) Estuary, East China Sea. Marine Chemistry 117(1–4): 2-10. doi: 10.1016/j.marchem.2009.02.008

Conflict of Interest

None declared.